

Article

# Graphitic Layered Structures Enhancing TiNT Catalyst Photo-Electrochemical Behaviour

Rosalba Passalacqua<sup>1,2,\*</sup>, Salvatore Abate<sup>1,2</sup>, Federica De Luca<sup>1</sup>, Siglinda Perathoner<sup>1,2</sup>  
and Gabriele Centi<sup>1,2</sup>

<sup>1</sup> Department of Chemical, Biological, Pharmaceutical and Environmental Sciences (ChiBioFarAm), University of Messina, 98166 Messina, Italy

<sup>2</sup> ERIC aisbl & INSTM CASPE (Laboratory of Catalysis for Sustainable Production & Energy), University of Messina, 98166 Messina, Italy

\* Correspondence: rpassalacqua@unime.it

**Abstract:** The increasing knowledge in nanoscience and materials technology promoted the development of advanced materials with enhanced and unusual properties suitable for sustainable applications ranging from energy to environmental purposes. Here are presented some results from our current investigations on composite semiconducting materials. The investigated composites have been prepared from different nitrogen precursors and thin films of TiO<sub>2</sub> nanotubes. The synergy between hetero-structures based on graphitic-C<sub>3</sub>N<sub>4</sub> and thin films of titania nanotubes obtained by anodisation was studied. The composites have been characterised with several complementary techniques to evidence the relation between photo-behaviour and the composition of the samples. This study allows new insights into the nature of the specific enhanced properties due to this synergy among the two compounds. The g-C<sub>3</sub>N<sub>4</sub>/TiNT heterojunctions showed enhanced photo-electrochemical properties observed from the photocurrent measurements. The as-prepared composites have been investigated as cathode materials in the electrocatalytic reduction of oxalic acid (OX), evidencing the capability of tuning the reaction toward glycolic acid with respect to the pristine TiNT array. The observed Faradic efficiency (FE) for the composites follows the trend: TiNT-U<sub>6</sub> > TiNT-M<sub>6</sub> > TiNT-MU<sub>18</sub>. TiNT-U<sub>6</sub> shows the best performances (FE<sub>CC</sub> = 63.7%; FE<sub>CO</sub> = 15.5%; OX conversion = 61.4%) after 2 h of reaction. The improved photo-electrochemical properties make these materials suitable for H<sub>2</sub> production, solar-light-driven water splitting, and CO<sub>2</sub> reduction applications.

**Keywords:** graphitic carbon nitrides; titania nanotubes; heterojunctions; nanocomposites; photocatalysts; visible light; photoelectrodes



check for updates

**Citation:** Passalacqua, R.; Abate, S.; De Luca, F.; Perathoner, S.; Centi, G. Graphitic Layered Structures Enhancing TiNT Catalyst Photo-Electrochemical Behaviour. *Coatings* **2023**, *13*, 358. <https://doi.org/10.3390/coatings13020358>

Academic Editor: Emerson Coy

Received: 24 December 2022

Revised: 24 January 2023

Accepted: 1 February 2023

Published: 4 February 2023



**Copyright:** © 2023 by the authors. Licensee MDPI, Basel, Switzerland. This article is an open access article distributed under the terms and conditions of the Creative Commons Attribution (CC BY) license (<https://creativecommons.org/licenses/by/4.0/>).

## 1. Introduction

In photocatalysis, many efforts have been made to improve materials performances by exploiting the deep research knowledge acquired in the last decades in materials science. In achieving progress in the development of materials, a powerful tool has been provided by the possibility of materials engineering at the nanoscale, coupled with the new knowledge and skills acquired by the recent intense and focused scientific research on these issues. Significant results have been obtained with composites, which often result in materials having new and unusual characteristics.

TiO<sub>2</sub> is one of the most widely utilised photocatalysts, as confirmed by the vast number of scientific papers concerning this material. One-third of the publications in heterogeneous photocatalysis of the last decade concern this catalyst. Thanks to the chemical stability, low toxicity, relative abundance, and low cost, it represents the most reliable choice despite some drawbacks related to the low absorption capability (band gap 3.2 eV) centred mainly in the UV region of solar radiation, which determines a low quantum efficiency, and the high rate of photogenerated charges recombination [1].

To improve and tailor the properties of this material for many applications ranging from environmental remediation to renewable energy conversion, the approaches adopting chemical modification, such as doping, functionalisation, interface engineering, etc., have evidenced effective results [2–5]. In each of these applications, aspects such as particle size and shape, crystal phase, surface morphology, and chemistry of the titania-based materials are the key parameters to be settled for the process optimisation [3,4]. By engineering the material structure of TiO<sub>2</sub>, some drawbacks of the traditional particle-size catalysts have been overcome by using 1D structures that have demonstrated superior charge transport capability [3,4]. Another fascinating recent field of material development concerns the modification of the energy band gap of the semiconductor through the coupling with suitable components to improve the titania visible light absorption response.

On the other hand, organic g-C<sub>3</sub>N<sub>4</sub> semiconductor polymer materials have emerged as one of the most versatile, metal-free, visible-light-activated photocatalysts, providing an inexpensive, nontoxic, abundant alternative to classical transition metal catalysts and organic dyes. The medium band gap of 2.7 eV, equivalent to 460 nm wavelength, causes g-C<sub>3</sub>N<sub>4</sub> to be active in the range of visible light. Recent studies have proposed using g-C<sub>3</sub>N<sub>4</sub> materials for various reduction reactions thanks to a suitable conduction band (CB) position. Its favourable CB level (significantly more negative than the conventional inorganic semiconductor counterparts) and the potentials of reactions, such as H<sub>2</sub> evolution, CO<sub>2</sub> reduction, and O<sub>2</sub> reduction, suggest that the electrons generated by light in g-C<sub>3</sub>N<sub>4</sub> have a great thermodynamic driving force to reduce several small molecules, such as H<sub>2</sub>O, CO<sub>2</sub>, and O<sub>2</sub>.

For example, carbon nitride/carbon nanodot hybrid composites (g-C<sub>3</sub>N<sub>4</sub>/CDs) [6] were proposed as photoactive layers to produce molecular hydrogen and oxygen (H<sub>2</sub> and O<sub>2</sub>) from overall water splitting as a promising means of renewable energy storage. The excellent stability and durability of the proposed g-C<sub>3</sub>N<sub>4</sub>/CDs nanocomposites and their earth-abundance indicate them as environmentally friendly and eligible photocatalysts for water splitting [7–9]. Optimised polymeric carbon nitrides have evidenced significantly higher apparent quantum yield (AQY) (57% and 10% at 420 nm and 525 nm, respectively) for H<sub>2</sub> evolution than in most previous experiments, as reported by Zhang et al. [10] by a procedure of co-condensation of urea and oxamide followed by post-calcination in molten salt. The resulting highly crystalline species presents a maximum p–p layer stacking distance of heptazine units of 0.292 nm, which improves lateral charge transport and interlayer exciton dissociation. At the same time, the addition of oxamide decreases the optical bandgap from 2.74 to 2.56 eV, enabling efficient photochemistry with green light.

Thanks to their excellent stability, adequate CB levels, harmlessness, and low price, the g-C<sub>3</sub>N<sub>4</sub>-based photocatalysts have attracted increasing interest in the selective photocatalytic reduction of CO<sub>2</sub> [11,12]. Various strategies have been used to enhance their performances. For instance, Yu et al. showed that the Pt content significantly influences both activity and selectivity of g-C<sub>3</sub>N<sub>4</sub> for photocatalytic reduction of CO<sub>2</sub> into CH<sub>4</sub>, CH<sub>3</sub>OH, and HCHO [13]. It was demonstrated that the Pt co-catalyst facilitates the interfacial electron transfer from g-C<sub>3</sub>N<sub>4</sub> to Pt NPs, lowering the overpotential for CO<sub>2</sub> reduction. More recently, Liu and coworkers obtained advances in product selectivity using g-C<sub>3</sub>N<sub>4</sub> nanosheets from the thermal delamination of bulk g-C<sub>3</sub>N<sub>4</sub> in air. It was shown that g-C<sub>3</sub>N<sub>4</sub> nanosheets with a band gap of 2.97 eV are selective for CH<sub>4</sub>, whereas bulk g-C<sub>3</sub>N<sub>4</sub> with a smaller band gap of 2.77 eV forms CH<sub>3</sub>CHO as the main product [14]. Another interesting example, for its industrial applicability, was reported by Sharma et al. [15], who presented a novel single-atom confinement strategy toward single ruthenium atoms dispersion over porous carbon nitride surface for CO<sub>2</sub> reduction to methanol.

The superior performance of g-C<sub>3</sub>N<sub>4</sub> as light harvesters makes them promising nanoscale components for photosynthetic devices [16,17].

Moreover, recent studies have extended the use of graphitic carbon nitrides to a wider range of chemical visible-light-driven reactions for mild conditions synthesis of valuable fine chemicals, which span from photocatalytic oxidation of small molecules [18] to C–C

and C-heteroatom coupling reactions [19] and other uses [20]. For instance, mesoporous graphitic carbon nitride (mpg-CN) was proposed to photo-catalyse the direct hydroxylation of benzene to phenol in the presence of  $H_2O_2$  under visible light irradiation [18].

Graphitic  $C_3N_4$ -based photocatalysts have demonstrated outstanding potential for the oxidation of aromatic compounds [21–24] and for forming C–C bonds [25]. For example, Wang et al. have shown that metal-free graphene sheet/ $g-C_3N_4$  nanocomposite could affect the selective photocatalytic oxidation of cyclohexane to cyclohexanone through the superoxide radical anion ( $\bullet O_2^-$ ) induced by  $O_2$  activation [26]. Ghosh et al. [19] proposed using organic semiconductor mesoporous graphitic carbon nitride (mpg-CN) in photoredox catalysis for synthetically important functionalisation of arenes and heteroarenes. The above considerations and the versatility of the materials based on carbon nitride make them an excellent high-performance choice for future photocatalytic applications to drive the sustainable synthesis [27] of high-value organic molecules, according to selective transformations hardly treated by traditional thermal catalysis.

Interestingly,  $g-C_3N_4$  has been exploited to treat emerging organic contaminants (EOCs) effectively. They have been used as catalysts in advanced oxidation processes (AOPs), one of the crucial techniques for EOCs removal based on highly reactive radicals for treating organic wastewater [28]. In addition, improving electron–hole pair separation has been reported to show better pollutant degradation efficiency [29]. Attractive solutions were obtained with hetero-structured photocatalysts. For instance, outstanding photocatalytic performance has been obtained via interface engineering [30,31]. MXene-induced interface electron separation capability has been successfully applied in Fenton-like catalysts for the degradation of organic pollutants, such as  $g-C_3N_4/Ti_3C_2/MoSe_2$  [32] or  $2D/2D \alpha-Fe_2O_3/g-C_3N_4$ , two representative examples of Z-scheme heterojunction materials [33]. In such systems, the  $g-C_3N_4$  networks act as a medium for electron transfer and an adsorption site for organic molecules, accelerating the persulfate activation. In addition,  $g-C_3N_4$ , thanks to its electron-rich N, can be an excellent support for improving MOFs' stability and catalytic efficiency [34]. Therefore, the appropriate electronic band structures of  $g-C_3N_4$  and the ability to adjust and tune the electronic properties of the final composite are the basis of the wide range of potential technological applications of these nanomaterials.

Traditionally titania nanotubes (TiNTs) have demonstrated their ability as electrodes for oxalic acid reduction [35,36]. Here, we report an exciting example of  $g-C_3N_4/TiNT$  composites as novel electrode materials able to improve TiNT performances. The composites behave as selective cathodic electrodes that produce glyoxylic acid (GO) and glycolic acid (GC), two high-added-value chemicals [37]. In the present work, the preparation, the chemical–physical, morphological, structural, and functional characterisation of the  $g-C_3N_4/TiO_2$  composite materials have been reported together with their application as a cathode in OX reduction reaction. In particular, by exploring materials' synergy for photocatalysis, the physico-chemical properties of the  $g-C_3N_4/TiNT$  heterostructures have been studied, and their photo-electrochemical behaviour compared. Moreover, the electrochemical tests with OX have evidenced the capability of tuning the reaction toward glycolic acid with respect to the pristine TiNT array.

The observed behaviours indicate that these hybrid nanomaterials can be more efficiently exploited in photocatalysis thanks to their enhanced properties.

## 2. Materials and Methods

### 2.1. Hetero-Structures Preparation

The  $g-C_3N_4/TiNT$  junctions have been synthesised in a two-step process: in the first step, the synthesis of  $TiO_2$  nanotube arrays by controlled anodic oxidation (AO) of a Ti foil was realised. In contrast, the decoration of the nanotubes with a  $g-C_3N_4$  layer occurred in a successive heating and condensation step (see Figure 1).

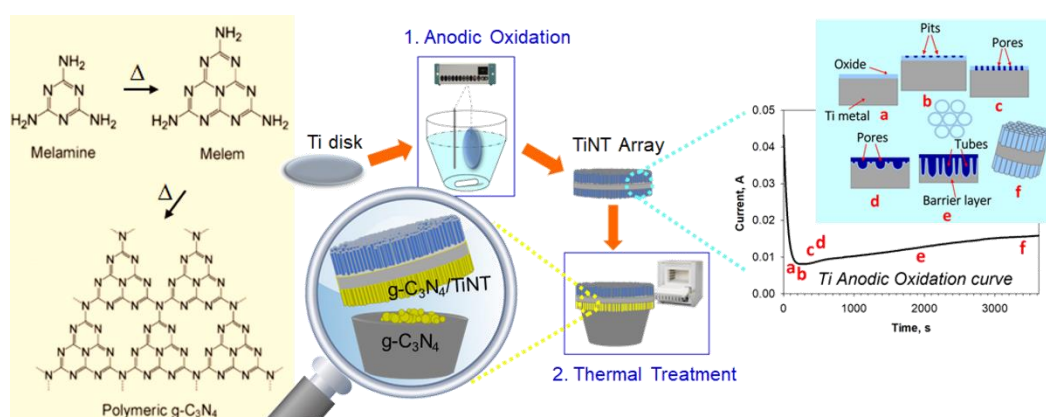


**Figure 1.** Scheme of the two-step  $g\text{-C}_3\text{N}_4/\text{TiNT}$  hetero-structures preparation [38]. A typical J-t curve recorded during anodic oxidation is shown in the insert on the left, along with the major changes (a–f) occurring in the metal substrate of Ti. On the left is the high-temperature self-polymerisation pathway of  $g\text{-C}_3\text{N}_4$  from melamine.

## 2.2. Synthesis of $\text{TiO}_2$ Nanotube Arrays

The preparation was prepared in a stirred electrochemical cell working at room temperature according to a standard procedure of controlled anodic oxidation [3,39]. Typically, a titanium disc (0.025 mm thickness, 35 mm diameter, 99.96% purity, Alfa Aesar, Kandel, Germany) was cleaned by sonication in deionised water, acetone, and isopropyl alcohol, sequentially, and then dried in an air stream. A self-organised  $\text{TiO}_2$  nanotube layer (approximately 2.2  $\mu\text{m}$  thick, as shown from SEM images) was grown on both sides of the metallic disc in ethylene glycol containing 0.3 wt%  $\text{NH}_4\text{F}$  and 0.2 vol.%  $\text{H}_2\text{O}$  at 50 V for 1 h.

## 2.3. Decoration of the Nanotube Arrays with $g\text{-C}_3\text{N}_4$

TiNTs decoration with  $g\text{-C}_3\text{N}_4$  was realised by a chemical vapour deposition (CVD) method using melamine, urea, or a 1:1 mixture of melamine–urea as the precursor [38,40]. A defined amount of precursor (6, 12, 18, or  $24 \cdot 10^{-3}$  mol) was placed in a ceramic crucible, and the disc of TiNTs was used as a cover. The TiNTs array was placed (top-down) above the precursor. The crucible was heated (heating and cooling rate 5  $^\circ\text{C}/\text{min}$ ) in a muffle at 550  $^\circ\text{C}$  for 3h, obtaining the deposition of the  $g\text{-C}_3\text{N}_4$  polymer onto the top of the crystalline structure of TiNTs. In contrast, some light-yellow  $g\text{-C}_3\text{N}_4$  powder was left in the crucible. The latter product was ground to a fine powder before being analysed. The term “back” is used to identify the side of the Ti disc on which the graphitic polymer was layered, while the other side not facing the inside of the crucible was named “front”. The proportion between  $g\text{-C}_3\text{N}_4$  and  $\text{TiO}_2$  nanotubes in each sample was controlled by modifying the initial amount of precursor (melamine, urea, or 1:1 melamine–urea mix) placed in the crucible. The tested samples are reported in Table 1 [38].

**Table 1.** Investigated samples and their characteristics of preparation [38].

Sample Name	Chemical Composition	Anodic Oxidation Parameters Potential (V) and AO Time (h)	$g\text{-C}_3\text{N}_4$ Precursor (mol)
TiNT	$\text{TiO}_2/\text{Ti}$	50; 1	-
TiNT-M <sub>6</sub>	$g\text{-C}_3\text{N}_4/\text{TiO}_2/\text{Ti}$	50; 1	Melamine $6 \times 10^{-3}$
TiNT-M <sub>12</sub>	$g\text{-C}_3\text{N}_4/\text{TiO}_2/\text{Ti}$	50; 1	Melamine $12 \times 10^{-3}$
TiNT-M <sub>18</sub>	$g\text{-C}_3\text{N}_4/\text{TiO}_2/\text{Ti}$	50; 1	Melamine $18 \times 10^{-3}$
TiNT-M <sub>24</sub>	$g\text{-C}_3\text{N}_4/\text{TiO}_2/\text{Ti}$	50; 1	Melamine $24 \times 10^{-3}$
TiNT-U <sub>6</sub>	$g\text{-C}_3\text{N}_4/\text{TiO}_2/\text{Ti}$	50; 1	Urea $6 \times 10^{-3}$
TiNT-U <sub>12</sub>	$g\text{-C}_3\text{N}_4/\text{TiO}_2/\text{Ti}$	50; 1	Urea $12 \times 10^{-3}$
TiNT-U <sub>18</sub>	$g\text{-C}_3\text{N}_4/\text{TiO}_2/\text{Ti}$	50; 1	Urea $18 \times 10^{-3}$

Table 1. Cont.

Sample Name	Chemical Composition	Anodic Oxidation Parameters Potential (V) and AO Time (h)	g-C <sub>3</sub> N <sub>4</sub> Precursor (mol)
TiNT-U <sub>24</sub>	g-C <sub>3</sub> N <sub>4</sub> /TiO <sub>2</sub> /Ti	50; 1	Urea $24 \times 10^{-3}$
TiNT-MU <sub>6</sub>	g-C <sub>3</sub> N <sub>4</sub> /TiO <sub>2</sub> /Ti	50; 1	1:1 Melamine–Urea $6 \times 10^{-3}$
TiNT-MU <sub>12</sub>	g-C <sub>3</sub> N <sub>4</sub> /TiO <sub>2</sub> /Ti	50; 1	1:1 Melamine–Urea $12 \times 10^{-3}$
TiNT-MU <sub>18</sub>	g-C <sub>3</sub> N <sub>4</sub> /TiO <sub>2</sub> /Ti	50; 1	1:1 Melamine–Urea $18 \times 10^{-3}$
TiNT-MU <sub>24</sub>	g-C <sub>3</sub> N <sub>4</sub> /TiO <sub>2</sub> /Ti	50; 1	1:1 Melamine–Urea $24 \times 10^{-3}$

#### 2.4. Chemical–Physical, Morphological, and Structural Characterisation of the g-C<sub>3</sub>N<sub>4</sub>/TiO<sub>2</sub> Composites

The crystallographic phases and structure of the g-C<sub>3</sub>N<sub>4</sub>/TiO<sub>2</sub> samples were determined by X-ray diffraction (XRD). The XRD spectra of the thin film samples of nanotubes coated with graphitic carbon nitride were carried out with a Philips X'Pert 3710 instrument using Cu K $\alpha$  radiation ( $\lambda = 0.154178$  nm, 30 kV, and 40 mA) under a glancing angle of 2°. Lower angles were used for a smaller sampling depth of the X-rays to maximise the intensity of reflections deriving from the thin film and minimise the contribution related to the underlying Ti substrate. Diffractograms were recorded over a 2 $\theta$  range of 10–80°.

The yellow powders of g-C<sub>3</sub>N<sub>4</sub> harvested in the crucible after the thermal condensation treatment for all the samples, except for urea-derived species at concentrations of 6, 12, and 18·10<sup>−3</sup> mol, were also analysed by a Bruker D2 Phaser desktop X-ray diffraction system (Bruker AXS GmbH, Karlsruhe, Germany) operating with the conventional Bragg–Brentano geometry. Diffraction peak identification was made by comparison to the patterns collected in the JCPDS database of reference compounds.

The micrographs of the composites and the corresponding CN<sub>x</sub> powders were acquired using a Phenom benchtop SEM (Alfatest, Cernusco sul Naviglio, Italy) to analyse their morphology.

Evidence regarding the formation of carbon nitride polymers and further insights on the nature of the surface of the g-C<sub>3</sub>N<sub>4</sub>/TiNT composites were acquired by X-ray photoelectron spectroscopy (XPS). XPS measurements were performed using PHI Versa Probe II equipment (Physical Electronics, Chanhassen, Minnesota, USA). The survey C1s, O1s, N1s, and Ti2p spectra were recorded using Al K $\alpha$  (1486.6 eV) X-ray source and an analyser pass energy of 23.5 eV and 117 eV for the high-resolution core-level spectra and the survey spectrum, respectively. The X-ray beam size was 100 microns at 25 W. The freshly prepared samples were loaded in the intro chamber, and when a target vacuum (10<sup>−7</sup> Pa) was reached, they were moved to the main chamber for analysis. Before the analysis, a charge neutralisation procedure was performed by simultaneous irradiation of samples using a low-energy electron beam and an ion beam before measuring the spectra. XPS peak position was referenced to Au metal foil (84.0 eV). The resulting peaks were analysed and deconvoluted using the Multipack Data Reduction Software (version 9.6.1.7, ULVAC-PHI, Inc., Chigasaki, Japan), employing a Shirley background curve.

#### 2.5. Functional Properties of the g-C<sub>3</sub>N<sub>4</sub>/TiNT Composites

UV-visible diffuse reflectance spectra were recorded using a Jasco V570 spectrometer (Jasco Inc., Easton, Maryland, USA) equipped with an integrating sphere for solid samples using BaSO<sub>4</sub> as a reference.

Tauc's plot method was used for material band gap determination of the g-C<sub>3</sub>N<sub>4</sub>/TiNT composites from the corresponding diffuse reflectance spectra.

Photo-electrochemical measurements were performed to evaluate the functional characteristics of the samples. Chronoamperometry experiments determined the currents under

dark and illuminated conditions. A three-electrode setup home-made reactor with a quartz window was used to perform room temperature measurements under frontal lighting using a 2049 AMEL potentiostat–galvanostat (AMEL, Milano, Italy). Pt wire as the counter, a saturated Ag/AgCl electrode as the reference, and the samples listed in Table 1 as the working electrode were used. All the tests were carried out in 0.5 M Na<sub>2</sub>SO<sub>4</sub> solution purged with N<sub>2</sub> at 0.1 V or 0 V vs. Ag/AgCl.

The used light source was a 300 W Xe arc lamp (Oriel Instrument, Irvine, California, USA). A set of lenses for light collection and focusing, a water filter to eliminate infrared radiation, and a set of filters to select the desired wavelength range for evaluating the photo-response were used. An AM 1.5 G filter was utilised for simulating solar radiation, whereas to cut wavelengths below 480 and 280 nm, the optical filters LSZ179 and LSZ178 (Lot-Oriel) were used, respectively.

The irradiance of the light source was measured using a spectroradiometer (Lot Oriel, model ILT950).

Potentiostatic plots were obtained using a positive bias of 0.1 V between the photoelectrode (working electrode) and the reference electrode. Several on–off cycles were recorded as generally reported for testing of reference photoactive materials, such as Degussa P25 titania.

### 2.6. Use of *g*-C<sub>3</sub>N<sub>4</sub>/TiNT in Electrocatalytic Reduction of Oxalic Acid

Aimed at reducing environmental impact, a technological transformation of industrial chemical processes is underway that follows two global trends: electrification and the shift towards raw materials derived from biomass. Developing new routes for utilising CO<sub>2</sub> emissions is a contemporary, hot topic for fulfilling political aims for reducing greenhouse gas release and renewable energy changeover. Within this context is the research program devoted to the electrochemical conversion of CO<sub>2</sub> to oxalic acid (OX), which aims to establish a new value chain in carbon dioxide utilisation by producing higher-value-added C2 products from oxalic acid, that is, a CO<sub>2</sub> intermediate. The as-prepared *g*-C<sub>3</sub>N<sub>4</sub>/TiNTs were tested as selective cathodic electrodes that produce glyoxylic acid (GO) and glycolic acid (GC), two high-added-value chemicals. There is a market interest towards these products because both are used industrially: GC is used in the polymers industries as a monomer to synthesise polyglycolic acid (PGA), a thermoplastic polymer; in textile industries as a tanning and whitening agent; and in the food industries as a flavouring agent [27], whereas GO is utilised to produce pharmaceuticals, personal care, agrochemicals, and cosmetics components. Therefore, a new electrochemical route, more sustainable than the traditional one, devoted to their production is highly desirable. In fact, producing them from CO<sub>2</sub> electrocatalytically can lead to a cost reduction, and the use of more environmentally friendly industrial operations also offers numerous advantages: (i) the substitution of fossil-derived products with bio-based products; (ii) the use of renewable energy sources and bio-based raw materials for the process; and (iii) a reduced carbon footprint for the overall process. We recently investigated the OX reduction via the electrochemical route in the frame of the EU OCEAN project (grant number ID 767798).

The OX reduction tests were carried out using an electrochemical flow cell with three electrodes. The investigated composites act as the working electrode (WE), a Pt wire as the counter (CE), and saturated Ag/AgCl as the reference (RE). For the description of the electrochemical operating system, please refer to De Luca et al. [41].

## 3. Results and Discussion

TiO<sub>2</sub> nanotube arrays were prepared according to a previously described standard [3,38]. While the *g*-C<sub>3</sub>N<sub>4</sub>/TiNT composites were obtained by following the polycondensation method in a single synthesis step, in addition to pyrolysis and condensation of nitrogen precursors, the crystallisation of the titania nanotube film also took place. The latter film was obtained in an amorphous form in the starting phase of anodic oxidation of the metallic titanium substrate. Melamine rearrangements induced the tris-*s*-triazine at approximately

390 °C, while condensation of this unit to the ending polymeric  $C_3N_4$  species occurred at approximately 520 °C [42].

X-ray diffraction provided information concerning crystallographic phases and structure of the prepared materials, confirming the formation of the typical graphite-like stacking of  $C_3N_4$  layers in all the samples [43,44].

Figure 2a shows the XRD pattern of: (i)  $MU_{24}$  and (ii)  $M_{24}$  obtained from  $g-C_3N_4$  powders, (iii)  $M_{18}$ , (iv)  $MU_{18}$ , and (v)  $U_{18}$  of the  $g-C_3N_4$ /TiNT composites, and (vi)  $TiO_2$  nanotubes array grown on Ti.

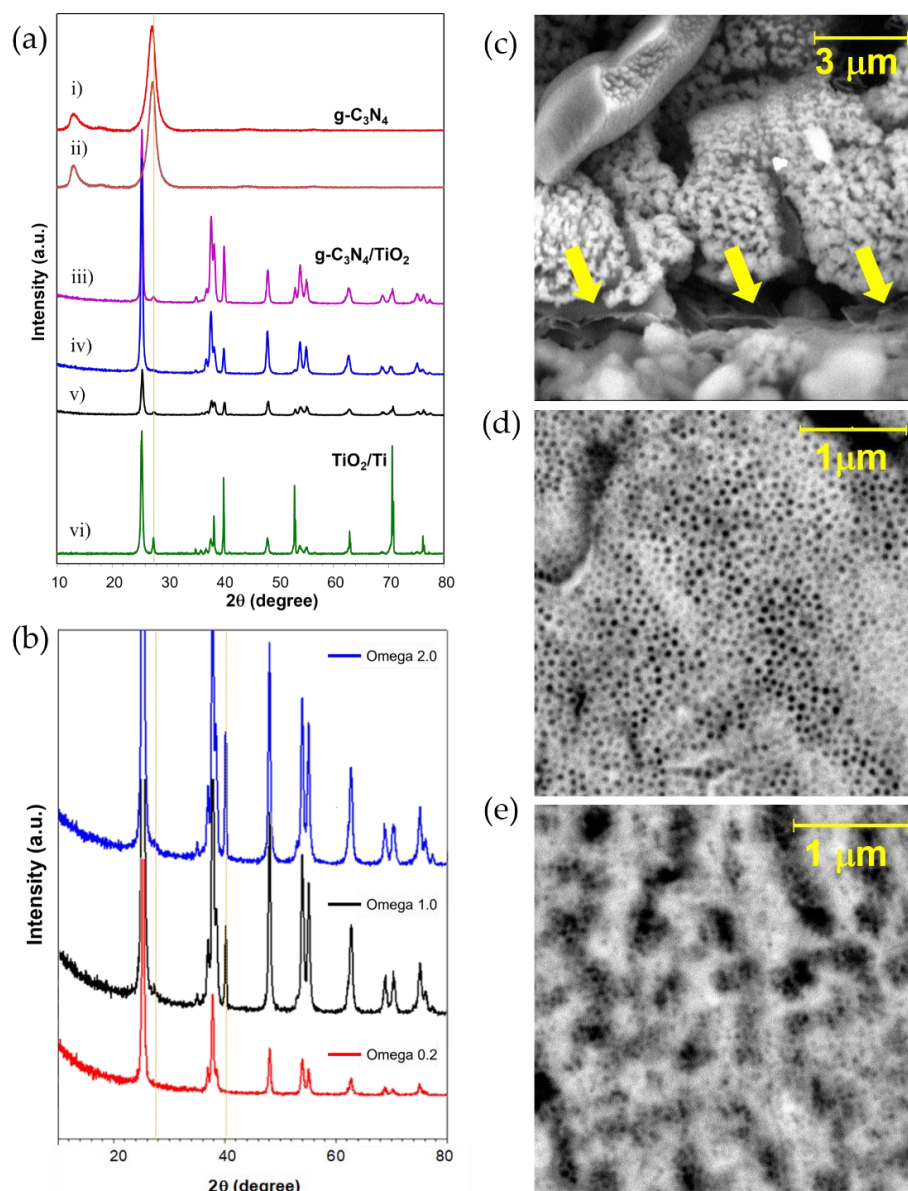


**Figure 2.** (a) XRD profiles. (i) and (ii)  $g-C_3N_4$  powders from  $MU_{24}$  and  $M_{24}$  precursors recovered in the crucible after the thermal treatment; (iii–v) Melamine-, Melamine–Urea-, and Urea- derived  $g-C_3N_4$ /TiNT- $U_{18}$  composites recorded with a  $2^\circ$  glancing angle; (vi) TiNT/Ti support [38]; (b) GAXRD patterns of the TiNT- $MU_{18}$  sample were recorded by decreasing the incident angle  $\omega$  from 2.0 to  $0.2^\circ$ . (c) SEM micrograph of  $g-C_3N_4$  powder obtained from  $18 \cdot 10^{-3}$  mol melamine precursor. The yellow arrows in (c) indicate the layered graphitic structures. SEM micrographs of (d) TiNT [38] and (e) TiNT- $M_{18}$  sample.

The pristine nanotube arrays consist mainly of anatase [3]. A low amount of rutile is present, and it is essentially located at the interface between TiNTs bottom and Ti substrate, as confirmed by the comparison of XRD recorded in glancing angle mode shown in Figure 2b. In fact, in the pattern of the TiNT-MU<sub>18</sub>, by decreasing the incident angle from 2.0° to 0.2° and, thus, the depth of penetration of X-rays, the diffraction peaks at ~27.5° and 40°, attributable to the rutile phase, disappear. Bare g-C<sub>3</sub>N<sub>4</sub> powders showed two peaks as observed in the XRD patterns of melamine, urea (not reported), and the equimolar ratio of the MU sample recovered in the crucible together with the corresponding composites. The first peak at 13.08° was assigned to the in-plane structural packing motif of the tri-s-triazine ring. It was indexed to (100) diffraction plane for graphitic materials [42]. The highest peak at 27.36° assigned as (002) diffraction plane was related to the interlayer stacking of the conjugated aromatic system. For graphitic C<sub>3</sub>N<sub>4</sub> prepared from 1:1 MU, the peaks were slightly shifted towards lower angles, 12.92° and 27.26°, with a significant broadening and a slight decrease in the overall intensity. The shifted peak position indicated an increment in both the in-plane nitride pores and the interlayer distance between the conjugated aromatic system, as previously reported by Martha et al. [44]. These features are characteristic properties of g-C<sub>3</sub>N<sub>4</sub> MU-derived species having conjugated aromatic layers that are well separated compared with the single precursor samples, TiNT-M<sub>18</sub> and TiNT-U<sub>18</sub>, which results in greater photocatalytic activity. In the diffraction pattern of the composites, the main peak at 25.38°, 25.42°, and 25.34° can be indexed to the (101) crystal plane of anatase (JCPDS file No. 21-1272), while the reflection of lower intensity found at 2θ values of 27.50°, 27.54°, and 27.50°, for M-, U- and MU- derivatives, respectively, can be indexed to the (110) crystal plane of rutile (JCPDS card No. 21-1276). Rutile diffraction signals presented a low intensity, and graphitic carbon signals fell almost at the same value of 2θ, so an overlap of the two diffraction peaks was possible. A detailed investigation highlighted that the rutile peak was located at 27.50°, and that of the g-C<sub>3</sub>N<sub>4</sub> system, correlated to the peculiar peak of the (002) crystal plane, was observed at 27.36°.

The samples' morphological characterisation by scanning electron microscopy (SEM) was performed (see Figure 2d for the TiNT-M18 composite and Figure 2e for the corresponding TiNT substrate). The comparison between the micrographs revealed that the pristine titania substrate showed tubes with open tops. At the same time, the composites were covered by stratified graphitic materials appearing as veiled tops surface. The typical CN<sub>x</sub> layered structures were more clearly visible in the bulk powder, as shown in Figure 2c and indicated by arrows.

XPS measurements investigated the electronic structure of the g-C<sub>3</sub>N<sub>4</sub>/TiNT composite materials to confirm the prepared samples' chemical composition and valence states. The survey spectra indicated the presence the Ti, O, C, and a small amount of N in all the prepared samples (see Figure 3), confirming that the target for the preparation procedure was achieved.

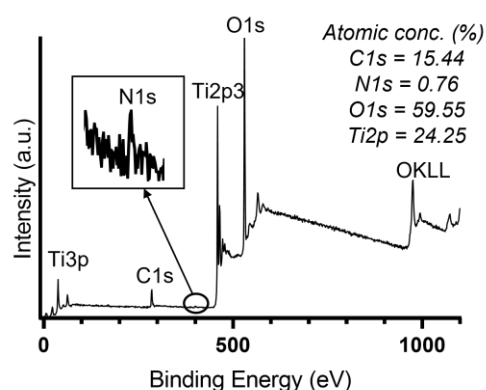
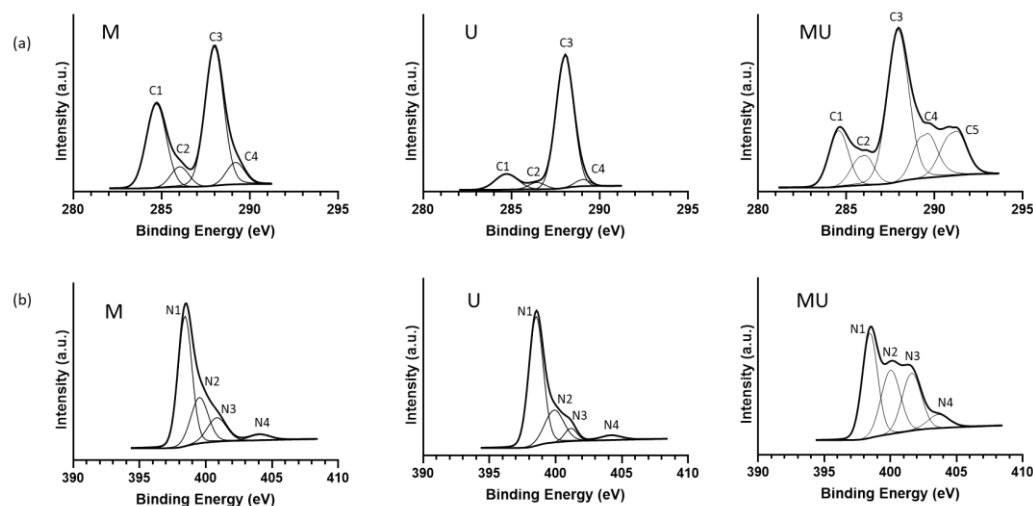


Figure 3. Survey XPS spectrum of the TiNT-U<sub>24</sub> composite.

Figure 3 reports the survey spectrum obtained for the TiNT-U<sub>24</sub> sample with the atomic percentages for the C, N, O, and Ti single components. All the other samples showed similar behaviour, but their spectra are not reported here for conciseness. For all the samples investigated, the amount of nitrogen was less than 1% wt. The electronic structure of the powder formed during the preparation of the composite electrodes was also investigated for the highest precursor concentration ( $24 \cdot 10^{-3}$  mol) for which it was possible to recover enough powder in the crucible after the preparation. The fitted C1s and N1s spectra of the powder samples are reported in Figure 4a,b, respectively. To describe the nature of the species, we refer to carbon nitride with the molecular formula C<sub>3</sub>N<sub>4</sub>.



**Figure 4.** XPS spectra for C<sub>3</sub>N<sub>4</sub> powder prepared from  $24 \cdot 10^{-3}$  mol precursor Melamine (M), Urea (U), and mixed precursor (MU): (a) C1s and (b) N1s.

All C1s spectra showed an asymmetric peak (C1) at a binding energy of 284.7 eV, assigned to C=C bonds in graphitic carbon. The large and stronger peak (C3) at 288.1 eV was due to N=C-N groups of triazine rings [45,46]. The large FWHM (1.35) of the C1 component indicated the presence of C atoms in highly defective sp<sup>2</sup> carbon phase and edge terminated C=N or C=O species [46]. Two minor peaks were observed by analysing the samples obtained with a single precursor. The first, C2 component at 286.2 eV, assigned to C=N or C=O in graphitic carbon, and the second, C4 component at 289.1 eV, due to the C-O, likely induced by the oxidation of the sample exposed to the air [45,47]. A higher amount of N=C-N species, approximately 80.3% (52% for the sample with melamine), at the expense of defective sp<sup>2</sup> graphite carbon, approximately 12.3% (32.7% for melamine) was observed using the urea precursor. The corresponding N1s (Figure 4b) showed four components assigned to pyridine-like C=N species (N1 species at 398.5 eV), conjugated amine C=N-H species (N2 at 399.8 eV), quaternary N (N3 at 401 eV), and a NO<sub>x</sub> species (N4 at 404 eV). This assignment is consistent with the literature [46] and indicates that the investigated material was a dispersed heptazine-based carbon nitride. When a mixed precursor was used, the C1s spectra showed a new component C5 at 291.0 eV assigned to a shake-up satellite observed in samples with high defective carbon sp<sup>2</sup> concentration [48]. The N1s spectra revealed a significant increase in the amount of C=N-H and quaternary N species at the expense of pyridine-like species C=N to the sample prepared with a single precursor, demonstrating that a more homogeneous N-species with a high concentration of defective sp<sup>2</sup> carbon phase were obtained by using a mixed precursor. Figure 5a shows the Ti2p spectra for the composites obtained with the highest precursor concentration ( $24 \cdot 10^{-3}$  mol) compared with the reference TiNT array. In all the composite materials, a shift at higher binding energy to pristine TiNT could be observed, indicating an interaction between the CN<sub>x</sub> and TiO<sub>2</sub> nanotubes. In the composites, the observed shift of the Ti signal indicated an interaction between the g-C<sub>3</sub>N<sub>4</sub> and TiNTs and an increased electron

density on Ti compatible with a charge transfer from the electron-rich  $g\text{-C}_3\text{N}_4$  surface to the unoccupied orbital of  $\text{Ti}^{4+}$  [49]. The observed shift for the  $\text{Ti}2p$  spectra in the composite materials with respect to TiNT suggests that a different interaction between  $\text{TiO}_2$  nanotubes and  $g\text{-C}_3\text{N}_4$  was achieved depending on the used precursor. This observation confirms the interaction between the two components and, ultimately, the effective preparation of the heterojunctions. The shift was approximately 0.23 eV with respect to TiNT for both TiNT-UM<sub>24</sub> and TiNT-U<sub>24</sub>, while for the TiNT-M<sub>24</sub> sample, the main peak of  $\text{Ti}2p$  was shifted 0.17 eV with respect to the TiNT reference.

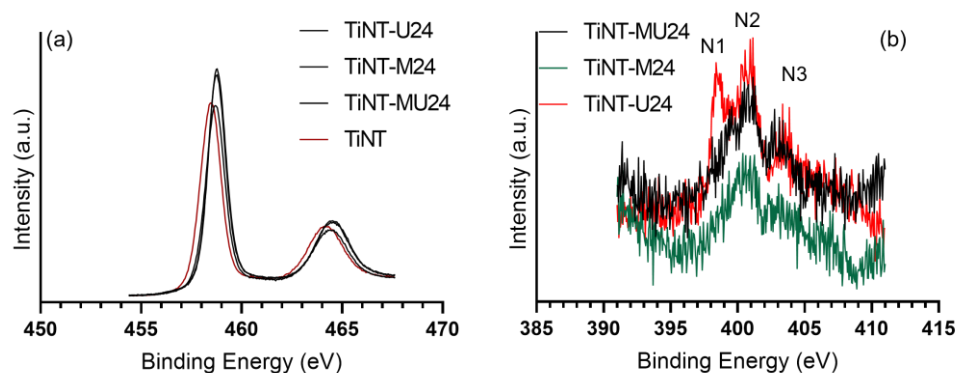


**Figure 5.** Comparison of (a)  $\text{Ti}2p$  and (b)  $\text{N}1s$  high-resolution XPS spectra for  $g\text{-C}_3\text{N}_4/\text{TiNT}$  composites prepared from  $24 \cdot 10^{-3}$  mol concentration of precursors.

Due to the low amount of N and, thus, low signal intensity, a deconvolution of  $\text{N}1s$  spectra was not feasible. Nonetheless, the spectra reported in Figure 5b, show the three main components N1, N2, and N3 as observed in the  $g\text{-C}_3\text{N}_4$  powder. It is important to note that these results are in accordance with those obtained in our previous paper by using a lower concentration of the precursors [41] and with the findings of similar systems reported in the literature [39,49]. For the analysis of the  $\text{O}1s$  signal in both pure TiNT and  $g\text{-C}_3\text{N}_4/\text{TiNT}$  samples, please refer to our previous paper [38].

The optical absorption properties of  $g\text{-C}_3\text{N}_4/\text{TiNT}$ s were investigated using UV-vis diffuse reflectance spectroscopy (see Figure 6).

To highlight the increasing performance of the TiNT covered with  $\text{CN}_x$  polymer, we collected the UV-vis DRS spectra and investigated the photocurrent behaviour of both sides of each sample. All the spectra recorded for the side facing the precursors showed a broad absorption shifted towards the visible region due to the presence of  $g\text{-C}_3\text{N}_4$  (see Figure 6b).

For the estimation of the optical band gap ( $E_g$ ), the following relation proposed by Tauc and further developed by Davis and Mott was used [50]:

$$(\alpha \cdot hv)^{1/n} = A(hv - E_g) \quad (1)$$

where  $h$  is the Planck's constant,  $v$  is the frequency of the incident photon,  $\alpha$  is the absorption coefficient,  $A$  is a proportional constant, and  $E_g$  is the band gap energy. The value of the exponent  $n$  indicates the nature of the electronic sample transition. For directly allowed transition  $n = 1/2$ , for direct forbidden  $n = 3/2$ , whereas for indirect, allowed transition  $n = 2$ , and indirect forbidden  $n = 3$ , respectively. In these systems,  $\alpha$  is not accessible; therefore, a robust well consolidated method can be used, which correlates the  $\alpha$  to the Kubelka–Munk function  $F(R_\infty) = \frac{(1-R_\infty)^2}{2R_\infty}$  by the measurement of the reflectance, which is proportional to the absorption coefficient [51]. Then, the  $\alpha$  in the Tauc equation was substituted with  $F(R_\infty)$ . Thus, the relation to be used becomes:

$$(F(R_\infty) \cdot hv)^{1/n} = A(hv - E_g) \quad (2)$$

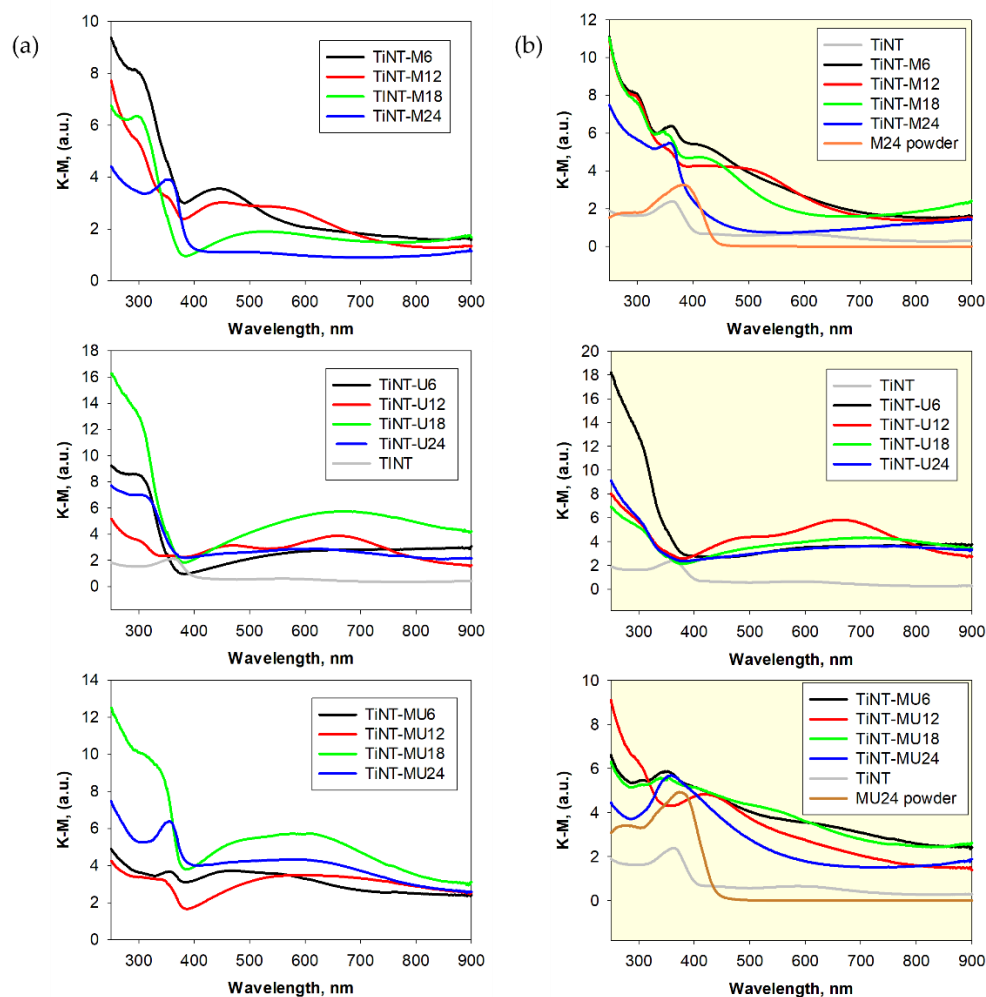


**Figure 6.** UV-vis spectra of TiNT reference, pure  $g\text{-C}_3\text{N}_4$  (from  $M_{24}$  and  $UM_{24}$  powders), and TiNT composites derived from melamine (M), urea (U), and (MU) precursor. Spectra recorded for: (a) the front side of each sample not facing the crucible and (b) the back side of each sample facing the inside of the crucible containing the precursor [38].

Equation (2) was modelled assuming an indirect ( $n = 2$ ) or direct ( $n = 1/2$ ) transition by plotting  $(F(R_\infty) \cdot hv)^{1/n}$  as a function of  $hv$ , the energy of incident photons. The intercept on the abscissa of the  $(F(R_\infty) \cdot E)^{1/n}$  vs.  $E$  provided the optical absorption edge energy value.

Following this procedure, the estimated  $E_g$  for pure  $g\text{-C}_3\text{N}_4$  (powders obtained with  $TiNT\text{-}M_{24}$  and  $TiNT\text{-}MU_{24}$ ) and for the TiNT support were 2.73, 2.97, and 3.13 eV, with the absorption edges at approximately 410 and 440 nm, respectively. Higher  $E_g$  values were obtained for the composites ranging between 2.19 and 3.64 eV. In particular, the calculated  $E_g$  were as follows: 3.54, 3.51, 3.55, and 3.19 eV for the  $TiNT\text{-}M_x$ , 3.65, 3.56, 3.52, and 3.63 eV for  $TiNT\text{-}U_x$ , respectively, whereas 3.48, 3.49, 3.64, and 2.62 eV for  $TiNT\text{-}MU_x$  with  $x$  increasing. The values of 3.48 and 3.64 eV, reported for  $TiNT\text{-}MU_6$  and  $TiNT\text{-}MU_{18}$ , respectively, were approximate due to the presence of low-intensity bands attributable to defective states. Figure 7 shows the Tauc graphs for the composites obtained with the highest concentration of precursors, and that of the TiNT substrate.

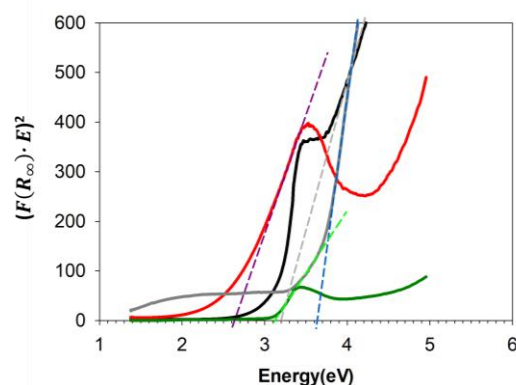


**Figure 7.** Tauc's plot was used to determine the investigated composites' optical bandgap.

For a closer investigation, the value obtained with Tauc's plot approach can be applied for all semiconducting materials that do not absorb light of the sub-band gap energy (or show a negligible absorbance). When used for materials showing a considerable absorbance at energies below  $E_g$ , the obtained results may be significantly distorted. It is the case for defective, doped, bulk, or surface-modified materials. All these modifications may introduce intraband gap states that reflect in the absorption spectrum as an Urbach tail, i.e., an additional, broad absorption band. In these cases, it must be taken into account to determine the band gap energy, otherwise the reported values could be underestimated [52]. An appropriate approach should involve the withdrawal of the g-C<sub>3</sub>N<sub>4</sub> spectrum from the spectral sum. Since, in this case, it was not possible to split the Kubelka–Munk spectrum into spectra of the individual components (TiNT and g-C<sub>3</sub>N<sub>4</sub>), a simplified procedure can be applied considering a linear fit also for the absorption below the fundamental so that the intersection between the two fitting lines gives the band gap energy estimation [52]. This baseline approach method was applied to estimate the energy gap of g-C<sub>3</sub>N<sub>4</sub>/TiNT composites. The  $E_g$  results for all the composites, obtained with the Tauc's plot and the baseline plotting method, where necessary, are reported in Table S1 in the supporting information.

Considering the fundamental mechanism of heterogeneous photocatalysis, the electronic properties of the composites have two main characteristics related to both improved separation (induced by the heterojunction construction) and migration of the charge carriers caused by the 2D geometry, in addition to the enhanced visible light harvesting. The construction of semiconductor heterojunctions, inducing band bending, can significantly boost the efficiency of spatial charge separation [53], enhancing the photocatalytic activity of g-C<sub>3</sub>N<sub>4</sub>-based composites. The geometry also favours higher densities of active surface sites. Moreover, the position of valence (VB) and conduction bands (CB) can be modulated on the basis of the C/N ratio, polymerisation degree, and crystallinity of the obtained materials. All these features result in enhanced superior performances of the composites.

Potentiostatic plots, performed by UV–vis radiation irradiation, highlighted a rapid photocurrent generation (see Figure 8). All the samples were photoactive, both under UV and visible light. The signals were generally stable after the five on–off cycles. A drop in the starting photocurrent was observed when performing the measurements with filters blocking portions of the incident UV–vis radiation. For TiNT-M<sub>6</sub>, utilising the AM1.5G filter, the photocurrent response was 24.1% of the initial value obtained under the full spectrum lamp irradiation; with UVB/C (LSZ179) and UVC (LSZ178) filters, the photocurrent was reduced to 66.6% and 27.8%, respectively (see Figure 8b).

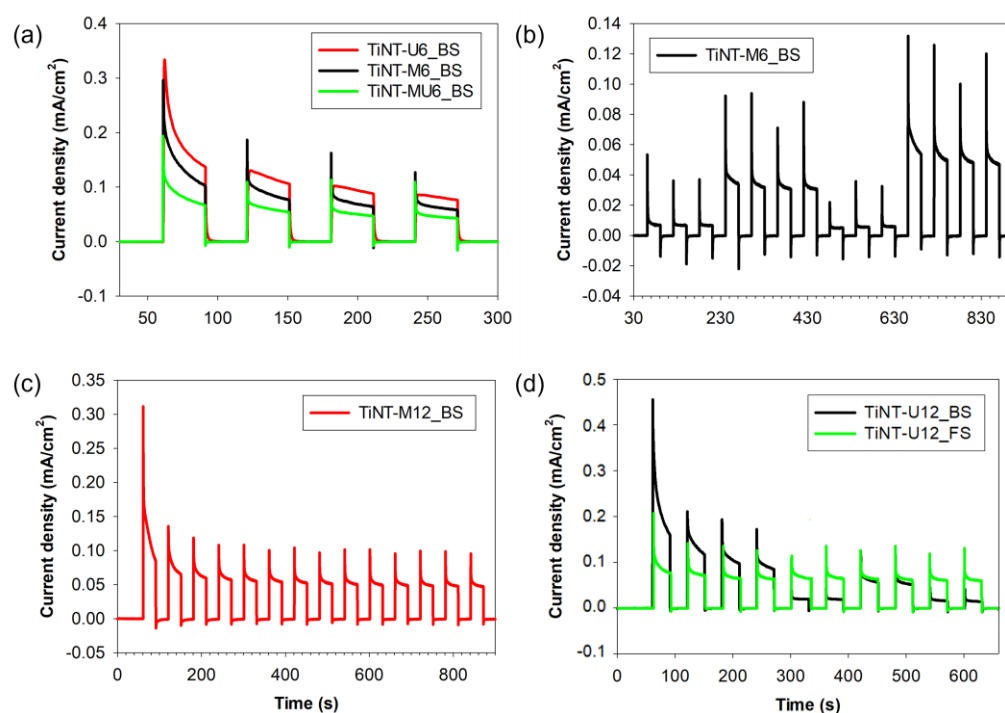


**Figure 8.** Chronoamperometric plot of (a) TiNT-M6, TiNT-U6, and TiNT-MU6 composites showing their different photocurrent responses under irradiation; (b) TiNT-M6 under different irradiations (recorded by using from left to right: UVC blocking, UVB/C blocking, and AM1.5G filter) and without filter (full Xe lamp spectrum), respectively; (c) Chronoamperometric plot of (c) TiNT-M12 highlighting the stability of the signal after the first five on–off cycles [38]; and (d) photocurrent response of the front (bare TiNT) and backside (covered by  $g\text{-C}_3\text{N}_4$ ) of the TiNT-U12 composite electrode, highlighting the signal increment in the 1–4 cycles (black line) for longer times (300–400s and 540–660s intervals), where the lower photocurrents are due to the use of UVC and UVB/C blocking filters, respectively.

The detected photocurrent responses were remarkably different depending on the sample's composition, with a greater photocurrent density for TiNT-MU18 than those of single precursor composites. In addition, by raising the precursor amount from 6 to  $18 \cdot 10^{-3}$  mol, an increase of photocurrent was usually observed, whereas, for the samples with the highest precursor concentration, a decrease in photocurrent response was noted. This trend is likely indicative of a saturation effect compatible with a thick  $g\text{-C}_3\text{N}_4$  layer covering the  $\text{TiO}_2$  nanotube surface (see UV-vis DRS in Figure 6 for comparison).

Dark–light cycles of the photoelectrode materials showed a swift increase in photocurrent and quick recovery to the original photocurrent signal through multiple on–off switches. After five cycles, the signal stabilised. Monitoring during discontinuous illumination showed the stability and reproducibility of the photocurrent in all the samples analysed (see Figure 8c) [38].

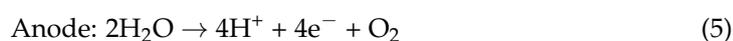
The observed photocurrents for the composite electrodes obtained from different concentrations of the same precursor decreased as follows:  $\text{TiNT-M}_{12} > \text{TiNT-M}_6 > \text{TiNT-M}_{18} > \text{TiNT-M}_{24}$ ;  $\text{TiNT-U}_{18} > \text{TiNT-U}_{12} > \text{TiNT-U}_6 > \text{TiNT-U}_{24}$ ;  $\text{TiNT-MU}_{18} > \text{TiNT-MU}_{12} > \text{TiNT-MU}_{24} \geq \text{TiNT-MU}_6$  for melamine, urea and 1:1 melamine/urea, respectively, while for the lowest precursor concentration, the observed trend was as reported in Figure 8a  $\text{TiNT-U}_6 > \text{TiNT-M}_6 > \text{TiNT-MU}_6$ .

The resulting composites exhibited photocurrent increments at least double that of the bare TiNT. Moreover, in all the cases, a marked difference was observed between the two sides of each disc, with a higher response for the back side (BS) on which the  $g\text{-C}_3\text{N}_4$  TiNT layer was deposited; an example is reported in Figure 8d. The most stable and intense current was observed for TiNT-MU18, whereas TiNT-M12 initially showed the

highest current increment after the recorded value stabilised at a level comparable to the one observed for TiNT-U<sub>18</sub>. The observed trends indicated that this type of hybrid material with improved properties can be advantageous in the field of photocatalysis, allowing a fine-tuning of their properties by selecting the appropriate precursor and its content during the preparation.

The prepared g-C<sub>3</sub>N<sub>4</sub>-TiNT composites were tested in an electrochemical flow cell for the electrocatalytic reduction of oxalic acid. They behaved as selective cathodic electrodes that produced glyoxylic acid (GO) and glycolic acid (GC).

The OX reduction is a two-step reaction. Firstly, (3) OX is reduced to GO in a two-electron process, then (4) GC is produced from GO through a further two-electron reduction step which involves the electrons coming from the water oxidation reaction (5) occurring at the anode side.



Our previous work investigated these electrodes at  $-1.1$  V and  $-1.3$  V vs. Ag/AgCl [41]. Afterwards, these working electrodes were tested at  $-1.2$  V vs. Ag/AgCl for 2 h, and some electrodes were tested for 4 h to study their stability. An overview of the results obtained in these new conditions is shown in Figure 9.

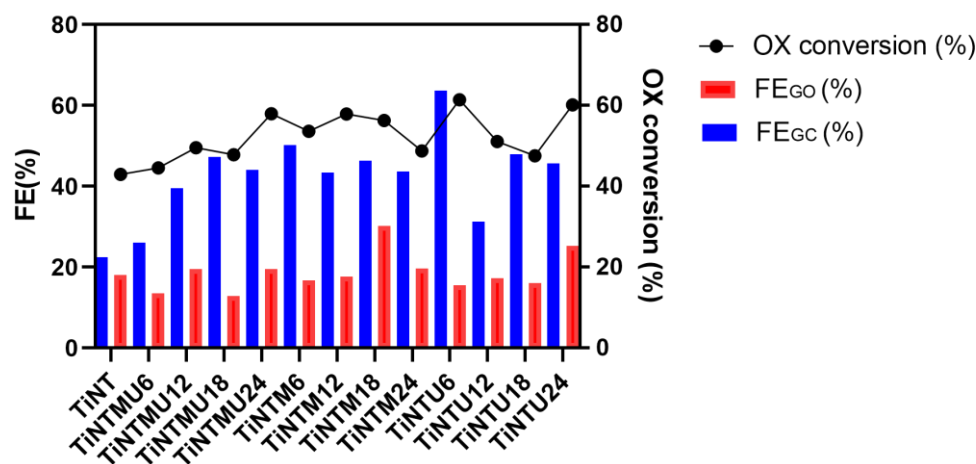


**Figure 9.** Efficiency to glyoxylic and glycolic acid of g-C<sub>3</sub>N<sub>4</sub>/TiO<sub>2</sub> composites and TiNT reference sample at the potential of  $-1.2$  V vs. Ag/AgCl after 2 h of reaction.

Figure 9 shows the Faradaic efficiencies (FE) to GO and GC as well as the OX combined conversions observed after 2 h of reaction. The results highlight an increase in the production of GC for all the composites with respect to pristine TiNT. The latter shows a comparable Faradaic efficiency to GO (FE<sub>GO</sub>) and lower Faradaic efficiency to GC (FE<sub>GC</sub>). The overview highlights that in terms of FE, the best composite for each precursor followed the trend: TiNT-U<sub>6</sub> > TiNT-M<sub>6</sub> > TiNT-MU<sub>18</sub>. TiNT-U<sub>6</sub> after 2 h showed the most outstanding performances, with a FE<sub>GC</sub> equal to 63.7% and a FE<sub>GO</sub> of 15.5%.

The trend observed for OX conversion highlights a higher value for TiNT-U<sub>6</sub>, followed by TiNT-MU<sub>24</sub> and TiNT-M<sub>12</sub>.

In an attempt to find a correlation between the OX conversion and the type and concentration of N-species present in the composites, we have reported in a graph (see Figure 10) the area of the signal of the N species (for U<sub>24</sub>, M<sub>24</sub>, and MU<sub>24</sub> powders) as detected in XPS measurements, as a function of OX conversion for all the investigated potentials ( $-1.1$ ,  $-1.2$ , and  $-1.3$  V).

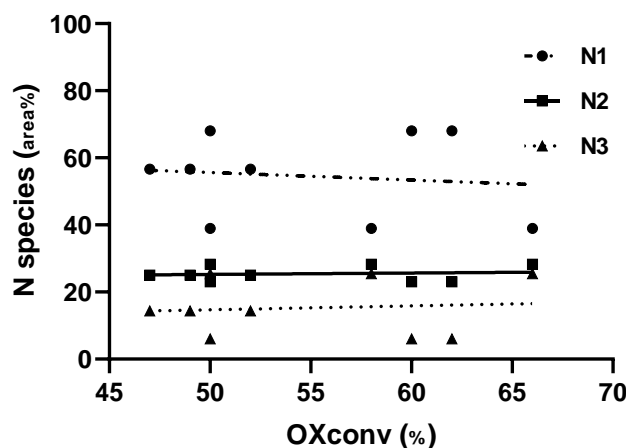


**Figure 10.** Correlation attempts between oxalic acid conversion as a function of N-species measured by XPS.

Although the low amount of N present on the composites and the availability of powders only for the highest precursor concentration ( $24 \cdot 10^{-3}$  mol) limited our investigation, from the graph, it seems that there is no correlation between the OX conversion and the amount of N-species detected in XPS spectra of  $24 \cdot 10^{-3}$  mol precursor. We can only observe that the N1 species seems detrimental to the conversion of OX, while the active species are individuated in N2 and N3. In particular, the conjugated amine  $C=N-H$  seems to be active in increasing the OX conversion. However, further investigations are required to understand how these species can affect the electronic properties of Ti nanotubes. Therefore, even if the correlation is not observable in this term, the electronic effect due to the presence of the N species is beyond doubt, as evidenced by the shift of the Ti XPS signal observed for the composite. In addition, it is confirmed by the different band gaps reported for the prepared sample.

#### 4. Conclusions

We have demonstrated the successful fabrication of carbon nitride materials with tunable properties depending on the composition and amount of the starting nitrogen precursor. The resulting materials exhibit improved optical absorption in the visible region and a better photo-electrochemical response than the single TiNT component. In the composite materials, the observed increments of photocurrent are at least double that of bare TiNT. Present trends indicate that this hybrid material with enhanced electronic properties can be advantageous in photocatalysis. Moreover, a recent study on using these materials as cathodes for oxalic acid reduction has been proposed. The main results highlight the capability of tuning the reaction toward glycolic acid with respect to the pristine TiNT array. The observed Faradic efficiency (FE) for the composites follows the trend:  $TiNT-U_6 > TiNT-M_6 > TiNT-MU_{18}$ .  $TiNT-U_6$  shows the best performances ( $FE_{GC} = 63.7\%$ ;  $FE_{GO} = 15.5\%$ ; OX conversion = 61.4%) after 2 h of reaction. The successful application of substrate electroreduction confirms the improved behaviour compared with the bare counterpart and the possibility of tuning the properties of the resulting composite depending on the selection of precursors and the amount of material used for the  $CN_x$  layers deposition. The obtained results represent a step forward for the design of next-generation materials needed to address the challenging area of “solar-driven chemistry and energy”.

**Supplementary Materials:** The following supporting information can be downloaded at: <https://www.mdpi.com/article/10.3390/coatings13020358/s1>, Table S1: Estimation of  $E_g$  with Tauc’s plot for the investigated composites, TiNT substrate, and the M24 and MU24 powders.

**Author Contributions:** Conceptualisation, R.P.; methodology, R.P.; software, R.P. and S.A.; validation, R.P.; formal analysis, R.P., S.A. and F.D.L.; investigation, R.P., S.A. and F.D.L.; resources, S.P.; data curation, R.P.; writing—original draft preparation, R.P.; writing—review and editing, R.P., F.D.L. and G.C.; visualisation, R.P. and S.A.; supervision, R.P.; project administration, S.P. and G.C.; funding acquisition, S.P. and G.C. All authors have read and agreed to the published version of the manuscript.

**Funding:** This research was funded from the MIUR under the PRIN2017 programme (project CO2 ONLY) and by the European Union's HORIZON2020 research and innovation program, grant number ID 767798 (OCEAN).

**Institutional Review Board Statement:** Not applicable.

**Informed Consent Statement:** Not applicable.

**Data Availability Statement:** Not applicable.

**Conflicts of Interest:** The authors declare no conflict of interest.

## References

1. Perathoner, S.; Passalacqua, R.; Centi, G.; Su, D.S.; Weinberg, G. Photoactive titania nanostructured thin films: Synthesis and characteristics of ordered helical nanocoil array. *Catal. Today* **2007**, *122*, 3–13. [[CrossRef](#)]
2. Passalacqua, R.; Perathoner, S.; Centi, G. Semiconductor, molecular and hybrid systems for photoelectrochemical solar fuel production. *J. Energy Chem.* **2017**, *26*, 219–240. [[CrossRef](#)]
3. Passalacqua, R.; Perathoner, S.; Centi, G. Use of modified anodisation procedures to prepare advanced TiO<sub>2</sub> nanostructured catalytic electrodes and thin film materials. *Catal. Today* **2015**, *251*, 121–131. [[CrossRef](#)]
4. Pang, Y.L.; Lim, S.; Ong, H.C.; Chong, W.T. A critical review on the recent progress of synthesising techniques and fabrication of TiO<sub>2</sub>-based nanotubes photocatalysts. *Appl. Catal. A Gen* **2014**, *481*, 127–142. [[CrossRef](#)]
5. Fan, B.-Y.; Liu, H.-B.; Wang, Z.-H.; Zhao, Y.-W.; Yang, S.; Lyu, S.-Y.; Xing, A.; Zhang, J.; Li, H.; Liu, X.-Y. Ferroelectric polarisation-enhanced photocatalytic performance of heterostructured BaTiO<sub>3</sub>@TiO<sub>2</sub> via interface engineering. *J. Cent. South Univ.* **2021**, *28*, 3778–3789. [[CrossRef](#)]
6. Liu, J.; Liu, Y.; Liu, N.; Han, Y.; Zhang, X.; Huang, H.; Lifshitz, Y.; Lee, S.-T.; Zhong, J.; Kang, Z. Metal-free efficient photocatalyst for stable visible water splitting via a two-electron pathway. *Science* **2015**, *347*, 6225. [[CrossRef](#)]
7. Perathoner, S.; Ampelli, C.; Chen, S.; Passalacqua, R.; Su, D.; Centi, G. Photoactive materials based on semiconducting nanocarbons—A challenge opening new possibilities for photocatalysis. *J. Energy Chem.* **2017**, *26*, 207–218. [[CrossRef](#)]
8. Zhang, G.; Li, G.; Lan, Z.-A.; Lin, L.; Savateev, A.; Heil, T.; Zafeiratos, S.; Wang, X.; Antonietti, M. Optimizing Optical Absorption, Exciton Dissociation, and Charge Transfer of a Polymeric Carbon Nitride with Ultrahigh Solar Hydrogen Production Activity. *Angew. Chem. Int. Ed.* **2017**, *56*, 13445–13449. [[CrossRef](#)]
9. Mishra, A.; Mehta, A.; Basu, S.; Shetti, N.P.; Reddy, K.R.; Aminabhavi, T.M. Graphitic carbon nitride (g-C<sub>3</sub>N<sub>4</sub>)-based metal-free photocatalysts for water splitting: A review. *Carbon* **2019**, *49*, 693–721. [[CrossRef](#)]
10. Low, J.; Yu, J.; Ho, W.J. Graphene-Based Photocatalysts for CO<sub>2</sub> Reduction to Solar Fuel. *Phys. Chem. Lett.* **2015**, *6*, 4244–4251. [[CrossRef](#)]
11. Marszewski, M.; Cao, S.; Yu, J.; Jaroniec, M. Semiconductor-based photocatalytic CO<sub>2</sub> conversion. *Mater. Horiz.* **2015**, *2*, 261–278. [[CrossRef](#)]
12. Yu, J.; Wang, K.; Xiao, W.; Cheng, B. Photocatalytic reduction of CO<sub>2</sub> into hydrocarbon solar fuels over g-C<sub>3</sub>N<sub>4</sub>-Pt nanocomposite photocatalysts. *Phys. Chem. Chem. Phys.* **2014**, *16*, 11492–11501. [[CrossRef](#)]
13. Niu, P.; Yang, Y.; Yu, J.C.; Liu, G.; Cheng, H.-M. Switching the selectivity of the photoreduction reaction of carbon dioxide by controlling the band structure of a g-C<sub>3</sub>N<sub>4</sub> photocatalyst. *Chem. Commun.* **2014**, *50*, 10837–10840. [[CrossRef](#)]
14. Sharma, P.; Kumar, S.; Tomanec, O.; Petr, M.; Chen, J.Z.; Miller, J.T.; Varma, R.S.; Gawande, M.B.; Zbořil, R. Carbon Nitride-Based Ruthenium Single Atom Photocatalyst for CO<sub>2</sub> Reduction to Methanol. *Small* **2021**, *17*, 2006478. [[CrossRef](#)] [[PubMed](#)]
15. Safaei, J.; Mohamed, N.A.; Noh, M.F.M.; Soh, M.F.; Ludin, N.A.; Ibrahim, M.A.; Isahak, W.N.R.W.; Teridi, M.A.M. Graphitic carbon nitride (g-C<sub>3</sub>N<sub>4</sub>) electrodes for energy conversion and storage: A review on photoelectrochemical water splitting, solar cells and supercapacitors. *J. Mater. Chem. A* **2018**, *6*, 22346–22380. [[CrossRef](#)]
16. Wen, J.; Xie, J.; Chen, X.; Li, X. A review on g-C<sub>3</sub>N<sub>4</sub>-based photocatalysts. *Appl. Surf. Sci.* **2017**, *391*, 72–123. [[CrossRef](#)]
17. Ye, I.; Cui, Y.; Qiu, X.; Wang, X. Selective oxidation of benzene to phenol by Fe-CN/TS-1 catalysts under visible light irradiation. *Appl. Catal. B Environ.* **2014**, *152*, 383–389. [[CrossRef](#)]
18. Ghosh, I.; Khamrai, J.; Savateev, A.; Shlapakov, N.; Antonietti, M.; König, B. Organic semiconductor photocatalyst can bifunctionalize arenes and heteroarenes. *Science* **2019**, *365*, 360–366. [[CrossRef](#)] [[PubMed](#)]
19. Ding, J.; Liu, Q.; Zhang, Z.; Liu, X.; Zhao, J.; Cheng, S.; Zong, B.; Dai, W.-L. Carbon nitride nanosheets decorated with WO<sub>3</sub> nanorods: Ultrasonic-assisted facile synthesis and catalytic application in the green manufacture of dialdehydes. *Appl. Catal. B: Environ.* **2015**, *165*, 511–518. [[CrossRef](#)]

20. Zhu, Y.; Liu, Y.; Ai, Q.; Gao, G.; Yuan, L.; Fang, Q.; Tian, X.; Zhang, X.; Egap, E.; Ajayan, P.M.; et al. In Situ Synthesis of Lead-Free Halide Perovskite–COF Nanocomposites as Photocatalysts for Photoinduced Polymerization in Both Organic and Aqueous Phases. *ACS Mater. Lett.* **2022**, *4*, 464–471. [[CrossRef](#)]
21. Dai, X.; Xie, M.; Meng, S.; Fu, X.; Chen, S. Coupled systems for selective oxidation of aromatic alcohols to aldehydes and reduction of nitrobenzene into aniline using CdS/g-C<sub>3</sub>N<sub>4</sub> photocatalyst under visible light irradiation. *Appl. Catal. B Environ.* **2014**, *158*, 382–390. [[CrossRef](#)]
22. Su, F.; Mathew, S.C.; Moehlmann, L.; Antonietti, M.; Wang, X.; Blechert, S. Aerobic Oxidative Coupling of Amines by Carbon Nitride Photocatalysis with Visible Light. *Angew. Chem. Int. Ed.* **2011**, *50*, 657–660. [[CrossRef](#)] [[PubMed](#)]
23. Zhang, P.; Gong, Y.; Li, H.; Chen, Z.; Wang, Y. Selective oxidation of benzene to phenol by FeCl<sub>3</sub>/mpg-C<sub>3</sub>N<sub>4</sub> hybrids. *RSC Adv.* **2013**, *3*, 5121–5126. [[CrossRef](#)]
24. Li, X.-H.; Baar, M.; Blechert, S.; Antonietti, M. Facilitating room-temperature Suzuki coupling reaction with light: Mott-Schottky photocatalyst for C-C-coupling. *Sci. Rep.* **2013**, *3*, 1743. [[CrossRef](#)]
25. Li, X.-H.; Chen, J.-S.; Wang, X.; Sun, J.; Antonietti, M. Metal-Free Activation of Dioxygen by Graphene/g-C<sub>3</sub>N<sub>4</sub> Nanocomposites: Functional Dyads for Selective Oxidation of Saturated Hydrocarbons. *J. Am. Chem. Soc.* **2011**, *33*, 8074–8077. [[CrossRef](#)]
26. Rosso, C.; Filippini, G.; Criado, A.; Melchionna, M.; Fornasiero, P.; Prato, M. Metal-Free Photocatalysis: Two-Dimensional Nanomaterial Connection toward Advanced Organic Synthesis. *ACS Nano* **2021**, *15*, 3621–3630. [[CrossRef](#)]
27. Wang, L.; Jiang, H.; Wang, H.; Show, P.L.; Ivanets, A.; Luo, D.; Wang, C. MXenes as Heterogeneous Fenton-like Catalysts for Removal of Organic Pollutants: A Review. *J. Environ. Chem. Eng.* **2022**, *10*, 108954. [[CrossRef](#)]
28. Ajiboye, T.O.; Kuvarega, A.T.; Onwudiwe, D.C. Graphitic carbon nitride-based catalysts and their applications: A review. *Nano-Struct. Nano-Objects* **2020**, *24*, 100577. [[CrossRef](#)]
29. Zou, J.; Liao, G.; Wang, H.; Ding, Y.; Wu, P.; Hsu, J.-P.; Jiang, J. Controllable interface engineering of g-C<sub>3</sub>N<sub>4</sub>/CuS nanocomposite photocatalysts. *J. Alloys Compd.* **2022**, *911*, 165020. [[CrossRef](#)]
30. Ismael, M. A review on graphitic carbon nitride (g-C<sub>3</sub>N<sub>4</sub>) based nanocomposites: Synthesis, categories, and their application in photocatalysis. *J. Alloys Compd.* **2020**, *846*, 156446. [[CrossRef](#)]
31. Zhou, Y.; Yu, M.; Zhan, R.; Wang, X.; Peng, G.; Niu, J. Ti<sub>3</sub>C<sub>2</sub> MXene-induced interface electron separation in g-C<sub>3</sub>N<sub>4</sub>/Ti<sub>3</sub>C<sub>2</sub> MXene/MoSe<sub>2</sub> Z-scheme heterojunction for enhancing visible light-irradiated enoxacin degradation. *Sep. Purif. Technol.* **2021**, *275*, 119194. [[CrossRef](#)]
32. Geng, Y.; Chen, D.; Li, N.; Xu, Q.; Li, H.; He, J.; Lu, J. Z-Scheme 2D/2D α-Fe<sub>2</sub>O<sub>3</sub>/g-C<sub>3</sub>N<sub>4</sub> heterojunction for photocatalytic oxidation of nitric oxide. *Appl. Catal. B Environ.* **2021**, *280*, 119409. [[CrossRef](#)]
33. Wang, L.; Luo, D.; Yang, J.; Wang, C. Metal-organic frameworks-derived catalysts for contaminant degradation in persulfate-based advanced oxidation processes. *J. Clean. Prod.* **2022**, *375*, 134118. [[CrossRef](#)]
34. Zhao, F.; Yan, F.; Qian, Y.; Xu, Y.; Ma, C. Roughened TiO<sub>2</sub> Film Electrodes for Electrocatalytic Reduction of Oxalic Acid to Glyoxylic Acid. *J. Electroanal. Chem.* **2013**, *698*, 31–38. [[CrossRef](#)]
35. Murcia Valderrama, M.A.; van Putten, R.J.; Gruter, G.J.M. The Potential of Oxalic–and Glycolic Acid Based Polyesters (Review). Towards CO<sub>2</sub> as a Feedstock (Carbon Capture and Utilization–CCU). *Eur. Polym. J.* **2019**, *119*, 445–468. [[CrossRef](#)]
36. Abramo, F.P.; De Luca, F.; Passalacqua, R.; Centi, G.; Giorgianni, G.; Perathoner, S.; Abate, S. Electrocatalytic production of glycolic acid via oxalic acid reduction on titania debris supported on a TiO<sub>2</sub> nanotube array. *J. Energy Chem.* **2022**, *68*, 669–678. [[CrossRef](#)]
37. Perathoner, S.; Centi, G. Catalysis for solar-driven chemistry: The role of electrocatalysis. *Catal. Today* **2019**, *330*, 157–170. [[CrossRef](#)]
38. Passalacqua, R.; Abate, S.; Perathoner, S.; Centi, G. Improved Nanocomposite Photoanodes by Controlled deposition of g-C<sub>3</sub>N<sub>4</sub> on Titania Nanotube Ordered Films. *Chem. Eng. Trans.* **2021**, *84*, 25–30. [[CrossRef](#)]
39. Ampelli, C.; Centi, G.; Passalacqua, R.; Perathoner, S. Synthesis of solar fuels by a novel photoelectrocatalytic approach. *Energy Environ. Sci.* **2010**, *3*, 292–301. [[CrossRef](#)]
40. Sun, M.; Fang, Y.; Kong, Y.; Sun, S.; Yu, Z.; Umar, A. Graphitic carbon nitride (g-C<sub>3</sub>N<sub>4</sub>) coated titanium oxide nanotube arrays with enhanced photo-electrochemical performance. *Dalton Trans.* **2016**, *45*, 12702–12709. [[CrossRef](#)]
41. De Luca, F.; Passalacqua, R.; Abate, S.; Abramo, F.P.; Perathoner, S.; Centi, G. Graphitic-C<sub>3</sub>N<sub>4</sub>/TiO<sub>2</sub> Nanotube Array as Cathodic Materials for the Electrocatalytic Reduction of Oxalic Acid. *Chem. Eng. Trans.* **2021**, *84*, 37–42. [[CrossRef](#)]
42. Thomas, A.; Fischer, A.; Goettmann, F.; Antonietti, M.; Müller, J.-O.; Schlögl, R.; Carlsson, J.M. Graphitic carbon nitride materials: Variation of structure and morphology and their use as metal-free catalysts. *J. Mater. Chem.* **2008**, *18*, 4893–4908. [[CrossRef](#)]
43. Liao, G.; Chen, S.; Quan, X.; Yu, H.; Zhao, H. Graphene oxide modified g-C<sub>3</sub>N<sub>4</sub> hybrid with enhanced photocatalytic capability under visible light irradiation. *J. Mater. Chem.* **2012**, *22*, 2721–2726. [[CrossRef](#)]
44. Martha, S.; Nashima, A.; Parida, K.M. Facile synthesis of highly active g-C<sub>3</sub>N<sub>4</sub> for efficient hydrogen production under visible light. *J. Mater. Chem. A* **2013**, *1*, 7816–7824. [[CrossRef](#)]
45. Yue, B.; Li, Q.; Iwai, H.; Kako, T.; Ye, J. Hydrogen production using zinc-doped carbon nitride catalyst irradiated with visible light. *Sci. Technol. Adv. Mater.* **2011**, *12*, 034401. [[CrossRef](#)] [[PubMed](#)]
46. Large, A.I.; Wahl, S.; Abate, S.; da Silva, I.; Delgado Jaen, J.J.; Pinna, N.; Held, G.; Arrigo, R. Investigations of Carbon Nitride-Supported Mn<sub>3</sub>O<sub>4</sub> Oxide Nanoparticles for ORR. *Catalysts* **2020**, *10*, 1289. [[CrossRef](#)]

47. Martin, D.J.; Qiu, K.; Shevlin, S.A.; Handoko, A.D.; Chen, X.; Guo, Z.; Tang, J. Highly Efficient Photocatalytic H<sub>2</sub> Evolution from Water using Visible Light and Structure-Controlled Graphitic Carbon Nitride. *Angew. Chem. Int. Ed.* **2014**, *53*, 9240–9245. [[CrossRef](#)] [[PubMed](#)]
48. Chen, X.N.; Wang, X.H.; Fang, D. A review on C1s XPS-spectra for some kinds of carbon materials. *Fuller. Nanotub. Carbon Nanostructures* **2020**, *28*, 1048–1058. [[CrossRef](#)]
49. Liu, C.; Wang, F.; Zhang, J.; Wang, K.; Qiu, Y.; Liang, Q.; Chen, Z. Efficient Photoelectrochemical Water Splitting by g-C<sub>3</sub>N<sub>4</sub>/TiO<sub>2</sub> Nanotube Array Heterostructures. *Nano-Micro Lett.* **2018**, *10*, 37. [[CrossRef](#)]
50. Tauc, J.; Grigorovici, R.; Vancu, A. Optical Properties and Electronic Structure of Amorphous Germanium. *Phys. Status Solidi B* **1966**, *15*, 627–637. [[CrossRef](#)]
51. Kubelka, P.; Munk, F. An article on optics of paint layers. *Z. Tech. Phys.* **1931**, *12*, 593–601.
52. Makuła, P.; Pacia, M.; Macyk, W. How To Correctly Determine the Band Gap Energy of Modified Semiconductor Photocatalysts Based on UV-Vis Spectra. *J. Phys. Chem. Lett.* **2018**, *9*, 6814–6817. [[CrossRef](#)] [[PubMed](#)]
53. Cao, S.; Low, J.; Yu, J.; Jaroniec, M. Polymeric Photocatalysts Based on Graphitic Carbon Nitride. *Adv. Mater.* **2015**, *27*, 2150–2176. [[CrossRef](#)] [[PubMed](#)]

**Disclaimer/Publisher’s Note:** The statements, opinions and data contained in all publications are solely those of the individual author(s) and contributor(s) and not of MDPI and/or the editor(s). MDPI and/or the editor(s) disclaim responsibility for any injury to people or property resulting from any ideas, methods, instructions or products referred to in the content.